Turan O, Yigit S, Liang R, Chakraborty N. Laminar mixed convection of power-law fluids in cylindrical enclosures with heated rotating top wall.
***International Journal of Heat and Mass Transfer* 2018, 124, 885-899.**

Laminar mixed convection of power-law fluids in cylindrical enclosures with heated rotating top wall

Osman Turan[1,2]✉, Sahin Yigit[1], Ruibin Liang[1], Nilanjan Chakraborty[1]

[1] School of Engineering, Newcastle University, Newcastle-Upon-Tyne, NE1 7RU, UK

[2] Department of Mechanical Engineering, Bursa Technical University, Bursa, 16310, TURKEY

✉corresponding author.

osman.turan@newcastle.ac.uk

ABSTRACT

Laminar mixed convection of inelastic non-Newtonian fluids obeying a power law model in a cylindrical enclosure with a heated rotating top cover has been investigated numerically in this study. The steady-state axisymmetric simulations have been carried out for a range of different nominal Reynolds, Prandtl, Richardson numbers (i.e. $500 \leq Re \leq 2000$; $10 \leq Pr \leq 500$ and $0 \leq Ri \leq 1$) and power-law index (i.e. $0.6 \leq n \leq 1.8$) for an aspect ratio (height/radius) of unity (i.e. $AR = 1.0$). It has been found that mean Nusselt number $\overline{Nu}$ increases as *Re* and *Pr* increase, whereas $\overline{Nu}$ decreases with increasing values of Ri for shear-thinning (i.e. $n < 1$), Newtonian (i.e.$n = 1$) and shear-thickening (i.e. $n > 1$) fluids. It has been also observed that the variation of $\overline{Nu}$ with n differs depending on the values of Re and Ri. For instance, for small values of Reynolds number, $\overline{Nu}$ exhibits a non-monotonic trend (i.e. increases before reaching a maximum followed by a decreasing trend) with increasing n for small values of Richardson number, whereas $\overline{Nu}$ monotonically increases with increasing values of n for high Richardson number cases. However, in the case of high Reynolds number, $\overline{Nu}$ increases with n before reaching a maximum value which is followed by a decreasing trend for all values of Ri considered here. Detailed physical explanations are provided for the influences of Re, Pr, Ri, and n on $\overline{Nu}$ based on an elaborate scaling analysis. Finally, the numerical findings have been used to propose a correlation for $\overline{Nu}$ for the ranges of Re, Pr, Ri, n considered here.

Keywords: Mixed convection, Power-law fluid, Rotating end wall, Richardson number, Prandtl number

NOMENCLATURE

a	[-]	Bridging function
AR	[-]	Aspect ratio ($AR = H/R$)
b	[-]	Bridging function
C	[-]	Correlation parameter
c_1, c_2, c_3	[-]	Correlation parameters
c_p	[J/kgK]	Specific heat at constant pressure
D	[-]	Correlation parameter
d_1, d_2, d_3	[-]	Correlation parameters
e_a	[-]	Relative error
f_1	[-]	Functions
g	[m/s^2]	Gravitational acceleration
Gr	[-]	Grashof number
h	[W/m^{2}K]	Heat transfer coefficient
H	[m]	Height of cylindrical enclosure
k	[W/mK]	Thermal conductivity
k_0,k_1	[-]	Correlation parameters
m_0,m_1	[-]	Correlation parameters
n	[-]	Power-law index
Nu	[-]	Nusselt number
$\overline{Nu}$	[-]	Mean Nusselt number
Pr	[-]	Prandtl number
q	[W/m^2]	Heat flux
R	[m]	Radius of cylindrical enclosure
Ra	[-]	Rayleigh number
Re	[-]	Reynolds number
Ri	[-]	Richardson number
T	[K]	Temperature
U	(m/s)	Characteristic velocity scales in radial direction
V	(m/s)	Characteristic velocity scales in tangential direction
y_0, y_1, y_2	[-]	Correlation parameters
α	[m^2/s]	Thermal diffusivity
β	[1/K]	Coefficient of thermal expansion
$\dot{\gamma}$	[1/s]	Shear rate
δ,δ_{th}	[m]	Hydrodynamic and thermal boundary layer thickness
θ	[-]	Non-dimensional temperature ($\theta = (T\text{-}T_C)/(T_H\text{-}T_C)$)
μ	[Ns/m^2]	Plastic viscosity

ν	[m^2/s]	Kinematic viscosity
ρ	[kg/m^3]	Density
τ	[N/m^2]	Shear stress
Ω	[1/s)	Angular velocity

Subscripts

C	Cold wall
eff	Effective value
H	Hot wall
max	Maximum value
nom	Nominal value
r	Radial direction
ref	Reference value
wf	Condition of the fluid in contact with the wall
z	Axial direction
ϕ	Tangential direction

Special characters

ΔT	[K]	Difference between hot and cold wall temperature (= (T_H-T_C))
$\Delta_{min,cell}$	[m]	Minimum cell distance
r	[-]	Grid expansion ratio

1. INTRODUCTION

Mixed convection in cylindrical enclosures with a rotating end wall has been extensively investigated [1-14] due to its wide ranging engineering applications such as in fluid machinery, heat exchangers with a rotating fluid, food and chemical processing. Most of the studies in the existing literature are restricted to the Newtonian Fluids (where the viscous stress is directly proportional to strain rate) [1-9]. However, relatively limited effort has been directed to the analysis of mixed convection of non-Newtonian fluids [10-14] (where there is a non-linear relation between viscous stress and strain rate) despite their immense practical importance in anaerobic digesters, bio-chemical synthesis and polymer processing, to name a few notable applications.

Laminar flow of Newtonian fluids in a cylindrical container with a rotating cover has been experimentally investigated by Vogel [1,2], Ronnenberg [3], and Bertela and Gori [4]. The formation of different vortical structure and vortex breakdown phenomenon in this configuration have been reported for different values of Reynolds number (i.e. $\Omega R^2/\nu$ where Ω is the angular speed and ν is the kinematic viscosity) and aspect ratio (i.e. height to radius ratio $AR = H/R$) of the enclosure [1-4]. Escudier [5] extended these findings to provide stability criterion for vortex breakdown. The formation of vortical structures in this configuration has been found to considerably affect the rate of heat transfer in Newtonian fluids [8, 9]. Moreover, the effects of Prandtl [8], Reynolds and Richardson numbers [9] on the flow pattern and heat transfer rate in cylindrical enclosures with a heated rotating top wall have also been investigated for an aspect ratio of unity (i.e. $AR = H/R = 1$). It has been found that the mean Nusselt number is a strong function of Prandtl number [8] and the advective transport weakens, while the diffusive transport strengthens with an increase in Richardson number [9].

Several studies also focused on the flow structure of non-Newtonian fluids [10-12] in cylindrical enclosures with a rotating end wall. Escudier and Cullen [10] analysed cylindrical enclosures experimentally with a rotating top cover for viscoelastic shear-thinning fluids (i.e. viscosity decreases with increasing strain rate

and strain rate is dependent on time for constant shear stress). Stokes and Boger [11] proposed a regime diagram for flow stability based on Reynolds and Elasticity numbers for viscoelastic fluids in cylindrical enclosures with a rotating cover. The influence of shear-thinning character of inelastic non-Newtonian fluids on vortex breakdown (observed by Vogel [1,2] and Escudier [5] for Newtonian fluids) in cylindrical enclosures with a rotating cover was analysed both experimentally and numerically by Böhme *et al.* [12] where the viscosity was approximated by a power-law in terms of the shear rate. Böhme *et al.* [12] developed an aspect ratio - Reynolds number ($AR - Re$) diagram, representing the domain of vortex breakdown for shear-thinning fluids.

It is worth noting that all these aforementioned studies for non-Newtonian fluid flows in cylindrical enclosures with a rotating cover [10-12] confirmed that the formation of vortical structures is significantly different for non-Newtonian fluids in comparison to that in the Newtonian fluids for the same set of values of nominal Reynolds number Re and aspect ratio AR [10-12]. The formation of vortical structures for non-Newtonian fluids in cylindrical enclosures with a rotating end wall also significantly affects the heat transfer rate. However, to date, only a few [13-14] studies concentrated on the heat transfer characteristics of non-Newtonian fluids in cylindrical enclosures with a rotating end wall. Traore *et al.* [13] investigated heat transfer characteristics of viscoelastic fluids in cylindrical enclosures with a rotating top cover. They have reported that the heat transfer rate due to temperature fluctuations in viscoelastic fluids might locally increase the rate of heat transfer up to 4 times in comparison to the corresponding value in the purely conduction regime [13].

The heat transfer characteristics of inelastic shear-thinning and shear-thickening fluids in cylindrical enclosures with a rotating end wall have not yet been analysed in the existing literature. This paper addresses this deficit by analysing the heat transfer characteristics of inelastic shear-thinning and shear-thickening fluids obeying the power-law model of viscosity in cylindrical enclosures with a rotating heated top cover. An extensive parametric analysis has been conducted for a range of different nominal Reynolds (i.e. $500 \leq$

$Re \leq 2000$), Prandtl (i.e. $10 \leq Pr \leq 500$), Richardson (i.e. $0 \leq Ri \leq 1$) numbers, and power-law index (i.e. $0.6 \leq n \leq 1.8$) for an aspect ratio of unity (i.e. $AR = H/R = 1$). The range of nominal Reynolds number (i.e. $500 \leq Re \leq 2000$) has been chosen based on previous experimental [1-4] and numerical [8-9] studies in such a manner that steady state laminar flow can be realised.

The main objectives of this analyses are;

1. To demonstrate the influences of Re, Pr, Ri, n on the flow patterns and mean Nusselt number $\overline{Nu}$ in the case of mixed convection of power-law fluids in cylindrical enclosures with a heated rotating top wall for an aspect ratio of unity (i.e. $AR = H/R = 1$).
2. To propose a correlation for the mean Nusselt number $\overline{Nu}$ based on a detailed scaling analysis for the range of Re, Pr, Ri and n considered in this analysis.

Mathematical background and numerical implementation related to this analysis will be presented in the next two sections. Following that, a scaling analysis will be provided in order to elucidate the expected influences of Re, Pr, Ri, n on the mean Nusselt number. Subsequently, results will be presented along with its discussion. Finally, the conclusions are drawn and main findings are summarised.

2. MATHEMATICAL BACKGROUND

According to the power-law model, the viscous stress tensor τ_{ij} is expressed as [15]:

$$\tau_{ij} = \mu_a e_{ij} = K(e_{kl}e_{kl}/2)^{(n-1)/2} e_{ij} \quad (1)$$

Here, $e_{ij} = (\partial u_i/\partial x_j + \partial u_j/\partial x_i)$ is the rate of strain tensor, K is the consistency and n is the power-law index and $\mu_a = K(e_{kl}e_{kl}/2)^{(n-1)/2}$ is the apparent viscosity. The apparent viscosity μ_a decreases (increases) with increasing shear rate for $n < 1$ ($n > 1$) and thus fluids with $n < 1$ ($n > 1$) are referred to as shear-thinning (shear-thickening) fluids, whereas $n = 1$ represents Newtonian fluids. According to the

Buckingham's pi theorem, one obtains: $Nu = f(Re, Pr, Ri, n)$ where the nominal Reynolds, Prandtl and Richardson numbers for power-law fluids are defined as [12]:

$$Re = \frac{R^2}{(K/\rho)\Omega^{n-2}};\ Pr = \frac{(K/\rho)\Omega^{n-1}}{\alpha};\ Ri = \frac{Gr}{Re^2} = \frac{g\beta\Delta T H^3}{\Omega^2 R^4} \tag{2}$$

where $Gr = g\beta\Delta T H^3/[(K/\rho)^2\Omega^{2n-2}]$ is the Grashof number. It is worth noting that in eq. 2, the nominal apparent dynamic viscosity μ_{nom} is taken to be $\mu_{nom} = K\Omega^{n-1}$. For the current investigation, the local heat transfer coefficient *h* is defined as:

$$h = |-k(\partial T/\partial z)_{z=0} \times 1/(T_{z=0} - T_{z=H})| \tag{3}$$

The mean heat transfer coefficient and the mean Nusselt number are evaluated as:

$$\bar{h} = \int_0^R 2\pi r h dr/\pi R^2\ ,\ \ \overline{Nu} = \bar{h}R/k \tag{4}$$

2.1. Governing equations and boundary conditions

For steady-state incompressible axisymmetric swirling flows the conservation equations in the cylindrical coordinate system take the following form:

Mass conservation equation

$$\frac{\partial u}{\partial r} + \frac{u}{r} + \frac{\partial w}{\partial z} = 0 \tag{5}$$

Momentum conservation equations

$$r: \quad \rho\left(u\frac{\partial u}{\partial r} - \frac{v^2}{r} + w\frac{\partial u}{\partial z}\right) = -\frac{\partial p}{\partial r} + \frac{\partial \tau_{zr}}{\partial z} + \frac{\partial \tau_{rr}}{\partial r} + \frac{\tau_{rr} - \tau_{\phi\phi}}{r} \tag{6i}$$

$$\phi: \quad \rho\left(u\frac{\partial v}{\partial r} + \frac{uv}{r} + w\frac{\partial v}{\partial z}\right) = \frac{\partial \tau_{r\phi}}{\partial r} + \frac{\partial \tau_{z\phi}}{\partial z} + \frac{2\tau_{r\phi}}{r} \tag{6ii}$$

$$z: \quad \rho\left(u\frac{\partial w}{\partial r} + w\frac{\partial w}{\partial z}\right) = -\frac{\partial p}{\partial z} + \rho g\beta\left(T - T_{ref}\right) + \frac{1}{r}\frac{\partial}{\partial r}(r\tau_{rz}) + \frac{\partial \tau_{zz}}{\partial z} \tag{6iii}$$

Energy conservation equation

$$\rho c_p\left(u\frac{\partial T}{\partial r} + w\frac{\partial T}{\partial z}\right) = k\left(\frac{1}{r}\frac{\partial T}{\partial r} + \frac{\partial^2 T}{\partial r^2} + \frac{\partial^2 T}{\partial z^2}\right) \tag{7}$$

where T_{ref} is the reference temperature for evaluating the buoyancy term $\rho g\beta\left(T - T_{ref}\right)$ in the momentum conservation equation in the vertical direction, and here T_{ref} is taken to be the cold (bottom) cover temperature T_C. In addition, thermo-physical properties (thermal conductivity, specific heat, consistency, etc.) are assumed to be constant and independent of temperature in this analysis for the sake of simplicity.

The numerical investigation has been carried out in an axisymmetric cylindrical container with a rotating top cover, which is schematically shown in Fig. 1. The aspect ratio (i.e. $AR = H/L$) of the cylindrical container is considered to be unity (i.e. $AR = 1.0$). The bottom and top covers of the cylindrical enclosure are kept at different constant temperatures ($T_{bottom} < T_{top}$), while the cylindrical surface is considered to be adiabatic in nature. The temperature difference between the top and bottom covers is kept small enough to ensure that Boussinesq approximation remains valid. The velocity components are identically zero due to the no-slip conditions and the impenetrability of the surface of the container.

2.2. Numerical implementation, grid-independency and benchmarking

In this study, a commercial package ANSYS-FLUENT, which has previously been utilised successfully for simulating both non-Newtonian [16] and Newtonian fluids [17], has been used. The governing equations (i.e. Eqs. 5-7) are solved iteratively in the framework of the finite-volume methodology by applying the aforementioned boundary conditions. The convective terms are discretised using a second-order upwind scheme, whereas the diffusive terms are discretised by a second-order central differencing scheme. The coupling between pressure and velocity is obtained using the well-known SIMPLE (Semi-Implicit Method for Pressure-Linked Equations) algorithm [18]. The criterion of convergence was taken to be 10^{-7} for all the relative (scaled) residuals. Thus the iterations are stopped when the magnitude of the fractional change of all primitive variables between two successive iterations is either smaller than or equal to 10^{-7}. The mean Nusselt number has been found to change insignificantly (i.e. under 0.1% by magnitude for values obtained for convergence criteria 10^{-7} and 10^{-8}) when the threshold for convergence criterion is reduced by a factor

of 10. Thus, a convergence criterion of 10^{-7} has been taken as a compromise between accuracy and computational time.

Three different non-uniform meshes M1 (75×75), M2 (150×150) and M3 (300×300) have been investigated, and the details of these meshes have been provided in Table 1. The numerical uncertainty for the mean Nusselt number (i.e. $\overline{Nu}$) in case of shear-thinning (i.e. $n = 0.6$), Newtonian (i.e. $n = 1.0$), and shear-thickening (i.e. $n = 1.8$) fluids for $Ri = 0.5$, $Re = 2000$ at $Pr = 100$ are presented in Table 1. Table 1 highlights that the maximum relative error level (i.e. e_a) between M2 (150×150) and M3 (300×300) is found to be smaller than 0.6 % for shear-thinning (i.e. $n = 0.6$), Newtonian (i.e. $n = 1.0$), and shear-thickening (i.e. $n = 1.8$) fluids. Based on this analysis, the simulations have been conducted using mesh M2 (150×150), which is found to be sufficient for providing high accuracy and computational efficiency.

In addition to the grid-independency study, the simulation results for Newtonian fluids have also been compared with the benchmark data reported by Iwatsu [9] for different Ri and Re values at $AR = 1$ and $Pr = 1$. It has been shown elsewhere (i.e. Fig. 2 of Turan et al. [14]) that an excellent agreement (i.e. maximum difference in mean Nusselt number values was found to be smaller than 1%) with benchmark values reported by Iwatsu [9] has been obtained. The numerical scheme used here was previously also validated earlier for laminar natural convection of power-law fluids in square enclosures, and interested readers are referred to Ref. [19] for further information in this regard.

It is also worth noting that minimum and maximum levels of μ are taken to be $\mu_{min} = 10^{-4}\mu_{n=1}$ and $\mu_{max} = 10^{4}\mu_{n=1}$ respectively where $\mu_{n=1}$ is the viscosity of the Newtonian fluid for the same nominal values of Reynolds, Richardson and Prandtl numbers. It has been checked that the range of μ obtained from the simulation remains within μ_{min} and μ_{max} , and the results remain independent of the choices of μ_{min} and μ_{max}.

3. SCALING ANALYSIS

A detailed scaling analysis is performed to explain the influences of Re, Pr, Ri, n on the mean Nusselt number $\overline{Nu}$. The wall heat flux can be scaled as:

$$q \sim k\frac{\Delta T}{\delta_{th}} \sim h\Delta T \tag{8}$$

where δ_{th} is the thermal boundary layer thickness. Using Eq. 8, the Nusselt number can be scaled as:

$$Nu \sim \frac{hR}{k} \sim \frac{R}{\delta_{th}} \sim \frac{R}{\delta} f_1(Re, Ri, Pr, n) \tag{9}$$

where f_1 is a function of Re, Pr, Ri, Ra and n, which accounts for the ratio of hydrodynamic to thermal boundary layer thicknesses (i.e. $\delta/\delta_{th} \sim f_1(Re, Ri, Pr, n)$).

In order to estimate the hydrodynamic boundary thickness δ, the order of magnitudes of inertial and viscous forces in the radial direction can be the equated:

$$\rho\frac{U^2}{R} \sim \frac{\tau}{\delta} \tag{10}$$

For power-law fluids, the shear stress can be scaled as $\tau \sim K\ (U/\delta)^n$ and thus Eq. 10 gives rise to:

$$\rho\frac{U^2}{R} \sim K\left(\frac{U}{\delta}\right)^n \frac{1}{\delta} \tag{11}$$

Using Eq. 11, the hydrodynamic boundary thickness δ can be estimated as:

$$\delta \sim (K/\rho)^{1/(n+1)}\ R^{\,1/(n+1)}\ U^{\,(n-2)/(n+1)} \tag{12}$$

Here, U is the characteristic velocity scale in the radial directions. The equilibrium of the order of magnitudes of the inertial and centrifugal forces in the radial direction yields: $U \sim \Omega R$ in the case of pure forced convection ($Ri = 0$). By contrast, a combination of the equilibrium of inertial and buoyancy forces in the vertical direction and continuity relation provides $U \sim \sqrt{g\beta\Delta TR}$ for $H/R = 1.0$ in the case of pure natural convection (i.e. $Ri \to \infty$). These two asymptotic limits have been utilised to estimate U as [14]: $U \sim a(\Omega R) + b\left(\sqrt{g\beta\Delta TR}\right)$ where $a = e^{-\theta_1 Ri}$ and $b = 1 - e^{-\theta_1 Ri}$ (with θ_1 being a parameter) ensure that

$U \sim (\Omega R)$ for small values of Ri (i.e. for forced convection) whereas one obtains $U \sim \sqrt{g\beta\Delta TR}$ for large values of Ri (i.e. for natural convection). It is important to appreciate here that U only represents the magnitude of the radial velocity scale. In this configuration buoyancy force may aid/oppose the effects of rotation depending on the thermal boundary conditions of the horizontal walls. The values of a and b can be modified depending on whether buoyancy force aids or opposes the effects of rotation by modifying θ_1 in $U \sim a(\Omega R) + b\left(\sqrt{g\beta\Delta TR}\right)$.

Using $U \sim a(\Omega R) + b\left(\sqrt{g\beta\Delta TR}\right)$, Eq. 12 can be recast as follows:

$$\frac{\delta}{R} \sim Re^{-1/(n+1)}\left(a + bRi^{1/2}\right)^{(n-2)/(n+1)} \tag{13}$$

Equation 13 gives different results based on different Ri values. For example, for fully forced convection (i.e. $Ri = 0$), Eq. 13 yields to:

$$\frac{\delta}{R} \sim Re^{-1/(n+1)} \tag{14i}$$

For $Ri \gg 1$ (when natural convection drives the thermal transport) that yields:

$$\frac{\delta}{R} \sim Re^{-1/(n+1)} Ri^{(n-2)/(2n+2)} \tag{14ii}$$

Equation 14ii indicates that the effects of rotation do not disappear even for very high Ri values for both shear-thinning (i.e. $n < 1$) and shear-thickening (i.e. $n > 1$) fluids. Finally, substituting Eq. 13 into Eq. 9 leads to the following scaling estimate for the mean Nusselt number:

$$\overline{Nu} \sim Re^{1/(n+1)}\left(a + bRi^{1/2}\right)^{(2-n)/(n+1)} f_1(Re, Ri, Pr, n) \tag{15}$$

The key findings of this scaling analysis are also summarised in Table 2.

4. RESULTS & DISCUSSION

4.1 Influence of nominal Reynolds number Re

The variation of the mean Nusselt number $\overline{Nu}$ with nominal Reynolds number Re for $Ri = 0.5$ at $Pr = 500$ is shown in Fig. 2 for shear-thinning (e.g. $n = 0.6$), Newtonian (i.e. $n = 1$) and shear-thickening (e.g. $n = 1.8$) fluids along with the contours of non-dimensional temperature $\theta = (T - T_C)/(T_H - T_C)$ and stream function (i.e.$\Psi = \psi/\alpha$) for representative cases. Figure 2 shows circulatory motion within the enclosure which remains qualitatively similar for the representative cases. Moreover, in all the representative cases the temperature remains uniform for the major part of the domain apart from the regions within the thermal boundary layers adjacent to the active top and bottom walls. It can be seen from Fig. 2 that $\overline{Nu}$ increases with increasing Re regardless of the values of n for a given set of values of Ri and Pr. This is consistent with the scaling estimates given by Eq. 15 which suggests that $\overline{Nu}$ increases with increasing Re for a given set of values of Ri, Pr and n. It is insightful to analyse the distributions of non-dimensional temperature $\theta = (T - T_C)/(T_H - T_C)$ and swirl velocity component $V_\phi = vH/\alpha$ to understand the influences of Re on the mean Nusselt number $\overline{Nu}$. The distributions of θ and V_ϕ along the vertical mid-plane ($r/R = 0.5$) for shear-thinning (e.g. $n = 0.6$), Newtonian (i.e. $n = 1$) and shear-thickening (e.g. $n = 1.8$) fluids are presented in Fig. 3 for $Ri = 0.5$ and $Pr = 500$ for different values of Re. The sharp changes in the non-dimensional temperature θ and V_ϕ near top and bottom walls (i.e. $z/H = 0$ and 1.0) are indicative of the thermal boundary layer and hydrodynamic boundary layer respectively. It is evident from Fig. 3 that the thermal boundary layer thickness on the bottom cover decreases with increasing Re for shear-thinning (e.g. $n = 0.6$), Newtonian (i.e. $n = 1$) and shear-thickening (e.g. $n = 1.8$) fluid cases. This is also consistent with the scaling estimate of δ_{th} given by Eq. 13. This thinning of the boundary layer with increasing Re leads to an increase in the magnitude of wall heat flux for both top and bottom covers (see Eqs. 8), which in turn gives rise to an increase in $\overline{Nu}$ as shown in Fig. 2. An increase in $\overline{Nu}$ with increasing Re is a reflection of the strengthening of advective transport. This can also be confirmed from the non-dimensional swirl velocity V_ϕ distribution in Fig.3, which demonstrates that V_ϕ increases significantly with increasing Re for a given set of values of Ri, Pr and n.

The strengthening of advective transport with increasing Re, which is observed in Figs. 2 and 3, can be explained by integrating convective thermal transport (i.e. Q_{conv}) through the boundary layer thickness on the bottom cover:

$$Q_{conv} = Q_{adv} + Q_{diff} = \int_0^{\delta} \rho c_p u \Delta T dz - \int_0^{\delta} k(\partial T/\partial r) dz \tag{16}$$

where Q_{adv} and Q_{diff} are contributions of advective and diffusive thermal transports, respectively, and they can be scaled as follows:

$$Q_{adv} = \int_0^{\delta} \rho c_p u \Delta T dz \sim \rho c_p U \Delta T \delta \tag{17i}$$

$$Q_{diff} = -\int_0^{\delta} k \left(\frac{\partial T}{\partial r}\right) dz \sim (k\Delta T)\frac{\delta}{R} \tag{17ii}$$

where δ is the hydro-dynamic boundary layer thickness on the horizontal walls. Substituting $U \sim a(\Omega R) + b\left(\sqrt{g\beta\Delta T R}\right)$ and using the scaling relation for δ from Eq. 13 in Eqs. 17i and 17ii yield the following scaling estimates for the magnitudes of Q_{adv} and Q_{diff}:

$$Q_{adv} \sim (k\Delta T)\, Pr\, Re^{n/(n+1)}\left(a + bRi^{1/2}\right)^{(2n-1)/(n+1)} \tag{18i}$$

$$Q_{diff} \sim (k\,\Delta T)\, Re^{-1/(n+1)}\left(a + bRi^{1/2}\right)^{(n-2)/(n+1)} \tag{18ii}$$

Equations 18i and 18ii indicate that Q_{adv} (Q_{diff}) strengthens (weakens) with increasing Re. This is reflected in the increases in $\overline{Nu}$ with increasing nominal Reynolds number Re, as can be seen from Figs. 2.

4.2 Influence of Richardson number Ri

The variation of $\overline{Nu}$ with Ri is shown in Fig. 4 for shear-thinning (e.g. $n = 0.6$), Newtonian (i.e. $n = 1$) and shear-thickening (e.g. $n = 1.8$) fluids at $Re = 2000$ and $Pr = 500$. For $Ri = 0$ (i.e. fully forced convection), the fluid flow is driven by inertial and viscous forces whereas, when $Ri > 0$ (i.e. mixed = natural + forced convection) fluid flow is driven by inertial, buoyancy and viscous forces. Moreover, the

rotating heated top cover represents a stable configuration (i.e. lighter hot fluid sits on top of heavier cold fluid). Therefore, the effects of natural convection are confined only close to the heated top cover. The effects of buoyancy strengthens with increasing Ri, and the competition between buoyancy and viscous forces govern the flow for large values of Ri. It can be seen from Fig. 4 that $\overline{Nu}$ decreases with increasing Ri for shear-thinning (e.g. $n = 0.6$), Newtonian (i.e.$n = 1$) and shear-thickening (e.g. $n = 1.8$) fluids. This can be explained in terms of the competition between buoyancy and viscous forces for large values of Ri. The contours of non-dimensional temperature θ and stream functions (i.e. $\Psi = \psi/\alpha$) are shown in Fig. 5 for different values of Ri at $Re = 2000$ and $Pr = 10^3$. It can be seen from Fig. 5 that a single main circulation (i.e. a single cell) is obtained for fully forced convection (i.e.$Ri = 0$), whereas another small cell appears in the corner of the domain in addtion to the main circulation as Ri increases. This change in the flow patterns modifies isotherms between hot and cold walls which also contributes to the reduction in $\overline{Nu}$ with increasing Ri. This behaviour is consistent with previous analyses by Iwatsu [9] for Newtonian fluids (i.e. $n = 1.0$).

Furthermore, Figure 6 shows the distributions of the non-dimensional swirl velocity component V_ϕ along the vertical mid-plane ($r/R = 0.5$) for different Ri and n values at $Re = 2000$ and $Pr = 500$. It can be seen from Fig. 6 that the magnitude of V_ϕ decreases with increasing Ri towards the bottom of the container, whereas it is insensitive to Ri near rotating top cover of the cylindrical container. Thus, the advective transport weakens with increasing Ri in this configuration, and that is reflected in the reduction in heat transfer rate (and the mean Nusselt number $\overline{Nu}$) with increasing Ri.

4.3 Influence of Prandtl number

The variations of $\overline{Nu}$ with Pr for shear-thinning (e.g. $n = 0.6$), Newtonian (i.e. $n = 1$) and shear-thickening (e.g. $n = 1.8$) fluids are shown in Fig. 7 for $Ri = 0.5$ and $Re = 2000$. Figure 7 shows that $\overline{Nu}$ increases with increasing Pr, which is an indication of the strengthening of the advective transport with an increase

in nominal Prandtl number, irrespective the value of n. This can further be confirmed from the contours of non-dimensional temperature θ and stream functions (i.e. Ψ) shown in Fig. 8 for different values of Pr at $Re = 2000$ and $Ri = 0.5$. It can be seen from Fig. 8 that the magnitude of Ψ increases with increasing Pr. This is indicative of the strengthening of the advective transport in the enclosure which leads to an increase in $\overline{Nu}$ (see Fig. 7). In order to provide physical insights into the behaviour of Pr dependence of $\overline{Nu}$, the distributions of non-dimensional the swirl velocity component V_ϕ along the vertical mid-plane ($r/R = 0.5$) are also shown in Fig. 9 for different values of Pr at $Ri = 0.5$ and $Re = 2000$. It can be seen from Fig. 9 that the thermal boundary layer thickness decreases with increasing Pr for shear-thinning (e.g.$n = 0.6$), Newtonian (i.e. $n = 1$) and shear-thickening (e.g. $n = 1.8$) fluids, which in turn acts to increase the mean Nusselt number $\overline{Nu} \sim R/\delta_{th}$. In addition to this, the magnitude of V_ϕ increases with increasing Pr, regardless of the n values. This indicates that the advective transport strengthens with increasing Pr, which leads to an increase in $\overline{Nu}$ (see Fig. 7). It is also worth noting that the scaling estimation given by Eq. 18i suggests that Q_{adv} strengthens with increasing Pr, which is consistent with the observations from Fig. 7.

4.4 Influence of power-law index n

The variations of mean Nusselt number $\overline{Nu}$ with n are shown in Fig. 10 for different values of Ri and Re at $Pr = 500$. Figure 10 shows that $\overline{Nu}$ exhibits a non-monotonic behaviour (i.e. increases with increasing n before reaching a maximum which is followed by a decreasing trend) with increasing n (except in $Re = 500$ and 1000 for $Ri \geq 0.3$). This can be explained by a scaling analysis for the viscous resistance in the flow domain. In the power-law fluids, the viscous resistance strengthens with increasing n which can be explained by estimating the effective viscosity. The effective viscosity can be estimated as:

$$\mu_{eff} \sim K\dot{\gamma}^{n-1} \tag{19}$$

Using the velocity scale $U \sim \Omega R(a + bRi^{0.5})$, Eq. 19 can be scaled as:

$$\mu_{eff} \sim K\left(\frac{U}{\delta}\right)^{n-1} \tag{20}$$

Using Eq. 13 in Eq. 20 yields:

$$\mu_{eff} \sim K\Omega^{n-1}\left[Re^{\frac{1}{n+1}}\left(a+bRi^{\frac{1}{2}}\right)^{\frac{3}{n+1}}\right]^{n-1} \sim \mu_{nom}\left[Re^{1/(n+1)}\left(a+bRi^{1/2}\right)^{3/(n+1)}\right]^{n-1} \quad (21)$$

Equation 21 suggests that the effective viscosity μ_{eff} increases in comparison to μ_{nom} with increasing n for a given set of values of Re and Ri (within the range of Re and Ri values considered here), which is an indication of the strengthening of viscous forces.

Using μ_{eff} it is possible to estimate effective Reynolds number Re_{eff} and effective Grashof number Gr_{eff} as:

$$Re_{eff} = \frac{\rho\Omega R^2}{\mu_{eff}} = Re^{\frac{2}{n+1}}\left(a+bRi^{\frac{1}{2}}\right)^{\frac{3(1-n)}{n+1}} \quad (22i)$$

$$Gr_{eff} = \frac{\rho^2 g\beta\Delta T H^3}{{\mu_{eff}}^2} = RiRe^{4/(n+1)}\left(a+bRi^{1/2}\right)^{6(1-n)/(n+1)} \quad (22ii)$$

Equation 22 suggests that Re_{eff} and Gr_{eff} decrease with increasing n and this tendency strengthens for increasing Ri, which is indicative of the weakening of inertial and buoyancy forces over viscous forces. However, the exponents of Re and $(a+bRi^{\frac{1}{2}})$ are such in Eqs. 18i and 18ii that Q_{adv} and Q_{diff} are expected to increase with increasing n for a given set of values of Re and Ri.

The contours of non-dimensional temperature θ and stream functions (i.e. Ψ) are shown in Fig. 11 for different n and values at $Re = 1000$, $Ri = 1.0$ and $Pr = 10$. It can be inferred from Fig. 11 that thermal transport occurs principally due to advection (i.e. main circulation cell on top of the domain and curved isotherms which are not parallel to horizontal walls) in addition to thermal diffusion. Figure 11 shows that the main circulation increasingly gets compressed in the direction to the top right corner for increasing n and thus the isotherms are horizontally stretched forming a horizontally stratified structure. This developes a well-mixed and high tmeperature fluid layer next to the top and side walls and this tendency is stronger

for greater values of n. This is indicative of the strentgenhening of the advective thermal transport and thereby the mean Nusselt number $\overline{Nu}$ increases with increasing n. The strengthening of Q_{adv} with increasing n can also be confirmed from the non-dimensional swirl velocity V_ϕ distribution in Fig.12 which demonstrates that the magnitude of V_ϕ increases significantly with increasing n when Re, Ri and Pr are kept unaltered.

For a combination of small values of Re (i.e. $Re = 500$ and 1000) and $Ri \geq 0.3$, the strengthening of Q_{adv} and Q_{diff} with increasing n is reflected in an increase in $\overline{Nu}$. This mechanism is principally responsible for an increase in $\overline{Nu}$ with increasing n before the mean Nusselt number reaches a maximum for $Ri < 0.3$ for $Re = 500$ and 1000 and all values of Ri for $Re = 2000$ but the decreases in Re_{eff} and Gr_{eff} with increasing n becomes dominant for large values of n, which leads to a decrease in $\overline{Nu}$ with increasing n. The effects of strengthening of Q_{adv} and Q_{diff} with increasing n counteract the reductions in Re_{eff} and Gr_{eff} in such a manner that the power-law exponent n_{max} where the maximum $\overline{Nu}$ is obtained decreases with decreasing Ri (see Fig. 10c).

4.5 The mean Nusselt number correlation

In the case of Newtonian fluids, the following Nusselt number correlation was proposed for this configuration by Turan *et al.* [14] in the parameter range given by $0 \leq Ri \leq 1$, $500 \leq Re \leq 3000$ and $10 \leq Pr \leq 500$:

$$\overline{Nu}_{n=1} = 1 + k_0 Re^{m_0} \tag{23}$$

where k_o and m_o are the correlation parameters in which are listed in Table 3. Based on the scaling estimation given by Eq. 15, a correlation for the mean Nusselt number for power-law fluids has been proposed here for $0 \leq Ri \leq 1$, $500 \leq Re \leq 3000$ and $10 \leq Pr \leq 500$ in the following manner:

$$\overline{Nu} = Re^{1/(n+1)}\left(a + bRi^{1/2}\right)^{(2-n)/(n+1)} f_1 \tag{24}$$

The expression for f_1 is presented in Table 4 and the parameter θ_1 is taken to be unity (i.e. $\theta_1 = 1.0$) for $a = e^{-\theta_1 Ri}$ and $b = 1 - e^{-\theta_1 Ri}$ in Eq. 24. The predictions of Eq. 24 are compared to the numerical data in Fig. 13 for Pr = 10, 100 and 500, which demonstrates that the correlation satisfactorily captures the qualitative variations of $\overline{Nu}$ with n for the range of Ri, Re and Pr analysed in this study. The correlation given by Eq. 24 has been found to approximate the numerical results at the level of average error of 5 %. It is also worth noting that Eq. 23 shows better prediction than Eq. 24 for Newtonian fluids (i.e. $n = 1$) for a combination of small Re and large Pr (i.e. $Re = 500, Pr = 500$) where Eq. 24 over predicts $\overline{Nu}$. Nevertheless, Eq. 24 provides comparable predictions as that of Eq. 23 for Newtonian fluids (i.e. $n = 1$) for the rest of the parameter range considered here (see Fig. 13).

5. CONCLUSIONS

The influences of Reynolds, Prandtl, Richardson numbers and power-law index on the mean Nusselt number in the case of steady-state laminar mixed convection of power-law fluids in cylindrical enclosures with a heated rotating top cover have been analysed based on numerical simulations and a detailed scaling analysis. The mean Nusselt number $\overline{Nu}$ has been found to increase with increasing Reynolds and Prandtl number for shear-thinning (i.e. $n < 1$), Newtonian (i.e. $n = 1.0$) and shear-thickening (i.e. $n > 1$) fluids due to the strengthening of the advective transport. By contrast, the mean Nusselt number $\overline{Nu}$ shows a decreasing trend with increasing Ri for shear-thinning (i.e. $n < 1$), Newtonian (i.e. $n = 1.0$) and shear-thickening (i.e. $n > 1$) fluids. It has been also found that in the case of low Reynolds number, $\overline{Nu}$ exhibits a non-monotonic trend (i.e. increases with increasing n before reaching a maximum followed by a decreasing trend) with increasing n for small values of Richardson number, whereas $\overline{Nu}$ monotonically increases with increasing n values for high Richardson number cases. However, in the case of high Reynolds number, $\overline{Nu}$ increases with n before reaching a maximum which is followed by a decreasing trend for all values of Ri considered here. Detailed physical explanations have been provided for the aforementioned power-law exponent, Reynolds, Prandtl and Richardson number dependences of the mean Nusselt number $\overline{Nu}$. The numerical

results have been utilised to propose a correlation for the mean Nusselt number, which has been found to capture the simulation results accurately for the range of the parameters considered here.

ACKNOWLEDGEMENT

This study was supported by the Newton Research Collaboration Programme and is hereby gratefully acknowledged.

REFERENCES

[1] H. U. Vogel, Experimentelle Ergebnisse über die laminare Strömung in einem zylindrischen Gahause mit darin rotieren-der Scheibe. MPI Bericht 6, (1968).

[2] H. U. Vogel, Rückströmungsblasen in Drallsströmungen. Festschrift 50 Jahre Max-Planck-Institut für Strömungsforschung 1925–1975, (1975).

[3] B. Ronnenberg, Ein selbstjustierendes 3-Komponenten-Laserdoppleranemometer nach dem Vergleichsstrahlverfahren, angewandt für Untersuchungen in einer stationaren sylinder-symmetrischen Drehströmung mit einem Rückstromgebiet. MPI Bericht 20, (1977).

[4] M. Bertela, F. Gori, Laminar flow in a cylindrical container with a rotating cover, J. Fluids Eng. 104 (1982) 31–39.

[5] M.P. Escudier, Observations of the flow produced in a cylindrical container by rotating endwall, Experiments in Fluids 2 (1984) 189–196.

[6] H.J. Lugt, H.J. Haussling, Axisymmetric vortex breakdown in rotating fluid within a container, Trans. ASME J. Appl. Mech. 49 (1982) 921–923.

[7] J.M. Lopez, Axisymmetric vortex breakdown: Part1. Confined swirling flow, J. Fluid Mech. 221(1990) 533–552.

[8] C.H. Lee, J.M. Hyun, Flow of a stratified fluid in a cylinder with a rotating lid, Int. J. Heat and Fluid Flow 20 (1999) 26–33.

[9] R. Iwatsu, Flow pattern and heat transfer of swirling flows in cylindrical container with rotating top and stable temperature gradient, Int. J. Heat and Mass Transfer 47 (2004) 2755–2767.

[10] M.P. Escudier, L. M. Cullen, Flow of a shear-thinning liquid in a cylindrical container with a rotating end wall, Experimental Thermal and Fluid Science 12 *(*1996) 381–387.

[11] J. R. Stokes and D. V. Boger, Mixing of viscous polymer liquids, Phys. Fluids 12(6) (2000) 1411–1416.

[12] G. Böhme, L. Rubart, M. Stenger, Vortex breakdown in shear-thinning liquids: experiment and numerical simulations, J. Non-Newtonian Fluid Mech. 45 (1992) 1–20.

[13] B. Traore, C. Castelain and T. Burghelea, Efficient heat transfer in a regime of elastic turbulence, Journal of Non-Newtonian Fluid Mechanics 223 (2015) 62–76.

[14] O. Turan, S. Yigit , and N. Chakraborty, Numerical investigation of mixed convection of Bingham fluids in cylindrical enclosures with heated rotating top wall, Int. J. Heat and Mass Transfer 108 (2017) 1850–1869.

[15] M. Lamsaadi, M. Naïmi, M. Hasnaoui, Natural convection of non-Newtonian power law fluids in a shallow horizontal rectangular cavity uniformly heated from below, Heat Mass Transfer 41 (2005) 239-249.

[16] R.J. Poole, R.P. Chhabra, Development length requirements for fully-developed laminar pipe flow of yield stress fluids, ASME J. Fluids Eng. 132 (3) (2010)034501.

[17] M. P. Escuider, J. O'Leary, R.J. Poole, Flow produced in a conical container by a rotating end wall, Int. J. of Heat and Fluid Flow 28 (2007) 1418-1428.

[18] S. V. Patankar, Numerical Heat Transfer and Fluid Flow, Hemisphere, Washington, D.C, 1980.

[19] O. Turan, A. Sachdeva, N. Chakraborty and R.J. Poole, Laminar natural convection of power-law fluids in a square enclosure with differentially heated side walls subjected to constant temperatures, J. Non-Newt. Fluid Mech. 166 (2011) 1049-1063.

Table 1. The details of the meshes and the relative error for the mean Nusselt number $\overline{Nu}$ for shear-thinning (i.e. $n = 0.6$), Newtonian (*i.e.* n = 1.0) and shear-thickening (i.e. $n = 1.8$) fluids for $Ri = 0.5$ and $Re = 2000$ at $Pr = 100$.

Mesh Details	M1 (75 × 75)	M2* (150 × 150)	M3 (300 × 300)
$\Delta_{min,cell}/R$	3.10×10^{-3}	1.55×10^{-3}	0.78×10^{-3}
r_e	1.0519	1.0307	1.0203
Relative Error	M1 (75 × 75)	M2* (150 × 150)	M3 (300 × 300)
$\overline{Nu}$ $(n = 0.6)$	10.673	10.547	10.485
e_a (%)	1.19	0.59	
$\overline{Nu}$ $(n = 1)$	23.559	23.314	23.195
e_a (%)	1.05	0.51	
$\overline{Nu}$ $(n = 1.8)$	26.338	26.082	25.962
e_a (%)	0.98	0.46	

* The mesh which is used for the numerical simulations.

Table 2. Summary of scaling analysis.

The balance between inertial and viscous forces			$\rho\frac{U^2}{R}\sim\frac{\tau}{\delta}$
Velocity scales			$V\sim\Omega R$ $U\sim a(\Omega R)+b\left(\sqrt{g\beta\Delta TR}\right)$ where $a=e^{-\theta_1 Ri}$ and $b=1-e^{-\theta_1 Ri}$
Shear stress			$\tau\sim K\,(U/\delta)^n$
Hydrodynamic boundary layer thickness			$\frac{\delta}{R}\sim Re^{-1/n+1}\left(a+bRi^{1/2}\right)^{(n-2)/(n+1)}$
Nusselt number			$\overline{Nu}\sim Re^{1/(n+1)}\left(a+bRi^{1/2}\right)^{(2-n)/(n+1)}f_1(Re,Ri,Pr,n)$
	$n\neq 1$	$Ri=0$	$\overline{Nu}\sim Re^{1/(n+1)}f_1(Re,Pr,n)$
		$Ri\gg 1$	$\overline{Nu}\sim Re^{1/(n+1)}Ri^{(2-n)/(2n+2)}f_1(Re,Ri,Pr,n)$

Table 3. Summary of the mean Nusselt number correlation for Newtonian fluids (n = 1).

$\overline{Nu}_{n=1} = 1 + k_0 Re^{m_0}$
$10 \le Pr < 100$ and $0 \le Ri \le 1$
$k_0 = (0.015 - 0.003lnPr) + (0.113lnPr - 0.164)\exp(-Ri(2.539 + 1.214lnPr))$
$m_0 = (0.746 - 0.022lnPr) + (0.367lnPr - 0.83)Ri^{(0.229lnPr - 0.046)}$
$100 \le Pr \le 500$ and $0 \le Ri \le 0.5$
$k_0 = (0.283lnPr - 0.947)\exp(-Ri(16.76 - 1.874lnPr))$
$m_0 = (0.742 - 0.02lnPr) + (1.65 - 0.172lnPr)Ri^{(0.9 + 0.023lnPr)}$
$100 \le Pr \le 500$ and $0.5 < Ri \le 1$
$k_0 = (0.065lnPr + 0.012)\exp(-Ri(4.187 + 0.161lnPr))$
$m_0 = (-0.188 + 0.135lnPr) + (0.793 - 0.025lnPr)Ri^{(0.107 + 0.137lnPr)}$

Table 4. Summary of the mean Nusselt number correlation for power-law fluids.

$\overline{Nu} = Re^{1/(n+1)}\left(a + bRi^{1/2}\right)^{(2-n)/(n+1)} f_1(Re, Ri, Pr, n)$ where $\theta_1 = 1.0$			
$f_1 = \dfrac{1 + y_0 Ri}{y_1 + y_2 Ri}$			
$n < 1$	$y_0 = Cn^D$	$C = \dfrac{c_1 + c_2 Re}{1 + c_3 Re}$	$c_1 = 1.4696 - 0.0180Pr^{0.7012}$ $c_2 = (1 - 0.0038Pr)/(7.7420Pr - 1457.330)$ $c_3 = (1 - 0.0455Pr)/(623.914 - 168.436Pr)$
		$D = \dfrac{d_1 - d_2 Re}{1 + d_3 Re}$	$d_1 = (1 - 0.0383Pr)/(6.6813 - 0.5891\mathrm{Pr})$ $d_2 = (1 - 7.3 \times 10^{-4} Pr)/(544.342 + 15.7612Pr)$ $d_3 = (1 - 0.0130Pr)/(10.7576Pr - 630.278)$
	$y_1 = Cn^D$	$C = \dfrac{c_1 Re}{c_2 + Re}$	$c_1 = 4.9333Pr^{-0.3672}$ $c_2 = (682.556 - 19.9507Pr)/(1 + 0.4392Pr)$
		$D = \dfrac{d_1 Re}{d_2 - Re}$	$d_1 = (1.7432 - 0.0679Pr)/(1 - 0.0373Pr)$ $d_2 = (191.036 - 3.1020Pr)/(1 - 0.0327Pr)$
	$y_2 = Cn^D$	$C = \dfrac{c_1 - c_2 Re}{1 - c_3 Re}$	$c_1 = 30.0671\exp(-0.0026\mathrm{Pr})$ $c_2 = (1 + 0.0015Pr)/(51.9584 + 0.8882Pr)$ $c_3 = (1 - 0.0501Pr)/(769.080 + 7.4718Pr)$
		$D = \dfrac{1 + d_1 Re}{d_2 + d_3 Re}$	$d_1 = (1 + 0.0017Pr)/(343.718 + 3.6700\mathrm{Pr})$ $d_2 = (-2.3585 - 0.0107Pr)/(1 + 0.0339Pr)$ $d_3 = (1 - 0.0427Pr)/(779.933\mathrm{Pr} - 9052.38)$
$n \geq 1$	$y_0 = Cn^D$	$C = c_1 + c_2 Re$	$c_1 = (1.3060 - 0.0075Pr)/(1 + 0.0039Pr)$ $c_2 = (1 - 0.0026Pr)/(1.0372Pr - 1317.99)$
		$D = \dfrac{d_1 + d_2 Re}{1 + d_3 Re}$	$d_1 = (1 - 0.0024Pr)/(0.0033\mathrm{Pr} - 0.9632)$ $d_2 = (1 - 0.0012Pr)/(1732.90 - 0.9744Pr)$ $d_3 = (1 - 0.0233Pr)/(19.8032\mathrm{Pr} - 1237.42)$
	$y_1 = Cn^D$	$C = c_1 Re^{c_2}$	$c_1 = (6.2254 + 0.0228Pr)/(1 + 0.0254Pr)$ $c_2 = (1 - 0.0084Pr)/(0.0671Pr - 7.9913)$
		$D = d_1 - d_2 Re$	$d_1 = (0.0114Pr - 1.4308)/(1 - 0.0081Pr)$ $d_2 = (1 - 0.0022Pr)/(12161.11 + 83.8789\mathrm{Pr})$
	$y_2 = Cn^D$	$C = c_1 - c_2 Re$	$c_1 = (32.7882 - 0.0535Pr)/(1 + 0.0306Pr)$ $c_2 = (1 - 0.0020Pr)/(0.9566Pr + 141.9)$
		$D = \dfrac{d_1 + d_2 Re}{1 + d_3 Re}$	$d_1 = (-2.1113 - 0.0774Pr)/(1 + 0.0295Pr)$ $d_2 = (1 - 0.0175Pr)/(438.699 - 6.2725\mathrm{Pr})$ $d_3 = (1 - 0.0125Pr)/(11.752Pr - 1005.57)$

FIGURE CAPTIONS

Fig. 1. Schematic diagram of simulation domain and boundary conditions.

Fig. 2. The variation of mean Nusselt number $\overline{Nu}$ with Reynolds number Re and representative contours of non-dimensional temperature θ and stream function (i.e.$\Psi = \psi/\alpha$) in the case of shear-thinning (i.e. n = 0.6), Newtonian (i.e. n = 1) and shear-thickening (i.e. n = 1.8) fluids for Ri = 0.5 at Pr = 500.

Fig. 3. The variation of non-dimensional temperature θ and swirl velocity component V_ϕ along the vertical mid-plane (i.e. r / R = 0.5) for different Re values for shear-thinning (i.e. $n = 0.6$), Newtonian (i.e. $n = 1$) and shear-thickening (i.e. $n = 1.8$) fluids cases at Ri = 0.5 and Pr = 500.

Fig. 4. The variation of mean Nusselt number $\overline{Nu}$ with Richardson number Ri in the case of shear-thinning (i.e. n = 0.6), Newtonian (i.e. n = 1) and shear-thickening (i.e. n = 1.8) fluids for Re = 2000 at Pr = 500.

Fig. 5. Contours of non-dimensional temperature θ and stream functions (i.e. $\Psi = \psi/\alpha$) for different values of Ri at $Re = 2000$ and $Pr = 10^3$.

Fig. 6. The variation of non-dimensional temperature θ and non-dimensional swirl velocity component V_ϕ along the vertical mid-plane (i.e. r / R = 0.5) for different Ri values for shear-thinning (i.e. $n = 0.6$), Newtonian (i.e. $n = 1$) and shear-thickening (i.e. $n = 1.8$) fluids cases at Re = 2000 and Pr = 500.

Fig. 7. The variation of mean Nusselt number $\overline{Nu}$ with Prandtl number Pr in the case of shear-thinning (i.e. n = 0.6), Newtonian (i.e. n = 1) and shear-thickening (i.e. n = 1.8) fluids for Ri = 0.5 at Re = 2000.

Fig. 8. Contours of non-dimensional temperature θ and stream functions (i.e. Ψ) for different values of Pr at $Re = 2000$ and $Ri = 0.5$.

Fig. 9. The variation of non-dimensional temperature θ and non-dimensional swirl velocity component V_ϕ along the vertical mid-plane (i.e. r / R = 0.5) for different Pr values for shear-thinning (i.e. $n = 0.6$), Newtonian (i.e. $n = 1$) and shear-thickening (i.e. $n = 1.8$) fluids cases at $Ri = 0.5$ and $Re = 2000$.

Fig. 10. The variation of mean Nusselt number $\overline{Nu}$ with power-law index n for different Ri values at Pr = 500: a) Re = 500, b) Re = 1000 and c) Re = 2000.

Fig. 11. Contours of non-dimensional temperature θ and stream functions (i.e. Ψ) for different n and values at $Re = 1000$, $Ri = 1.0$ and $Pr = 10$.

Fig. 12. The variation of non-dimensional swirl velocity component V_ϕ along the vertical mid-plane (i.e. r / R = 0.5) for different n values for $Re = 500$ (left column) 2000 (right column) for $Ri = 0.1$ and 1.0 at $Pr = 500$.

Fig. 13. Comparison between $\overline{Nu}$ obtained from the simulations with the predictions of Eq. 23 (only for Newtonian fluids) and 24 for both Newtonian (i.e. $n = 1$) and power-law fluids for different Ri, Re and Pr.

TABLE CAPTIONS

Table 1. The details of the meshes and the relative error for the mean Nusselt number $\overline{Nu}$ for shear-thinning (i.e. $n = 0.6$), Newtonian (*i.e.* $n = 1.0$) and shear-thickening (i.e. $n = 1.8$) fluids for $Ri = 0.5$ and $Re = 2000$ at $Pr = 100$.

Table 2. Summary of scaling analysis.

Table 3. Summary of the mean Nusselt number correlation for Newtonian fluids ($n = 1$).

Table 4. Summary of the mean Nusselt number correlation for power-law fluids.

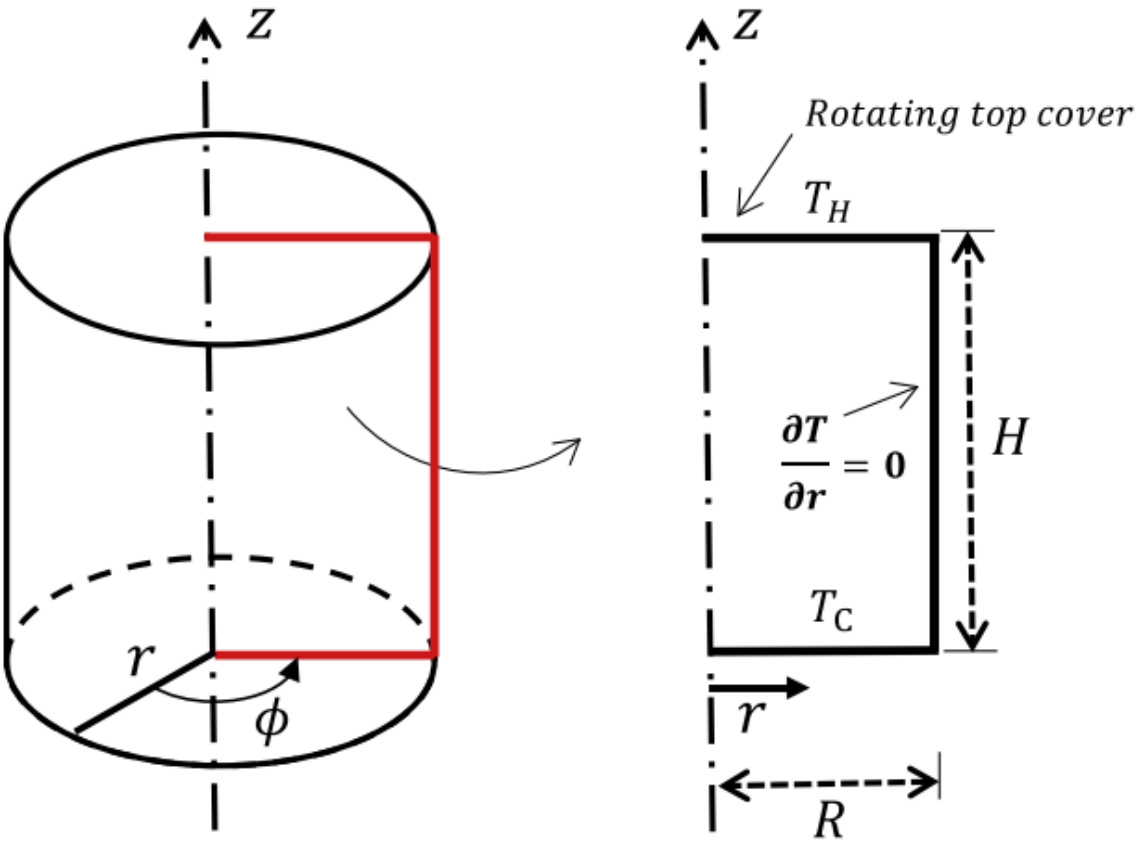

Fig.1. Schematic diagram of simulation domain and boundary conditions.

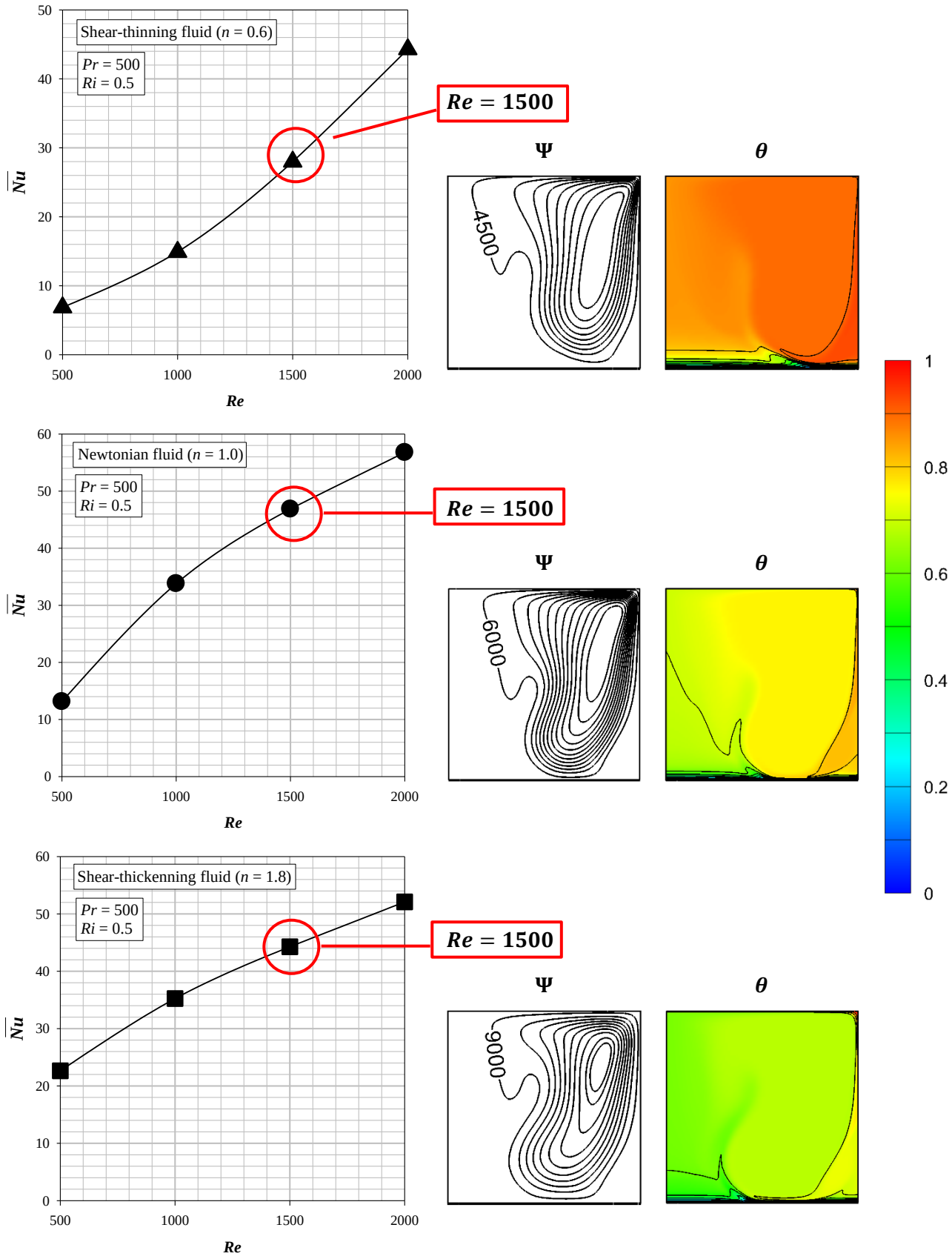

Fig. 2. The variation of mean Nusselt number $\overline{Nu}$ with Reynolds number Re and representative contours of non-dimensional temperature θ and stream functions (i.e. $\Psi = \psi/\alpha$) in the case of shear-thinning (i.e. n = 0.6), Newtonian (i.e. n = 1) and shear-thickening (i.e. n = 1.8) fluids for Ri = 0.5 at Pr = 500.

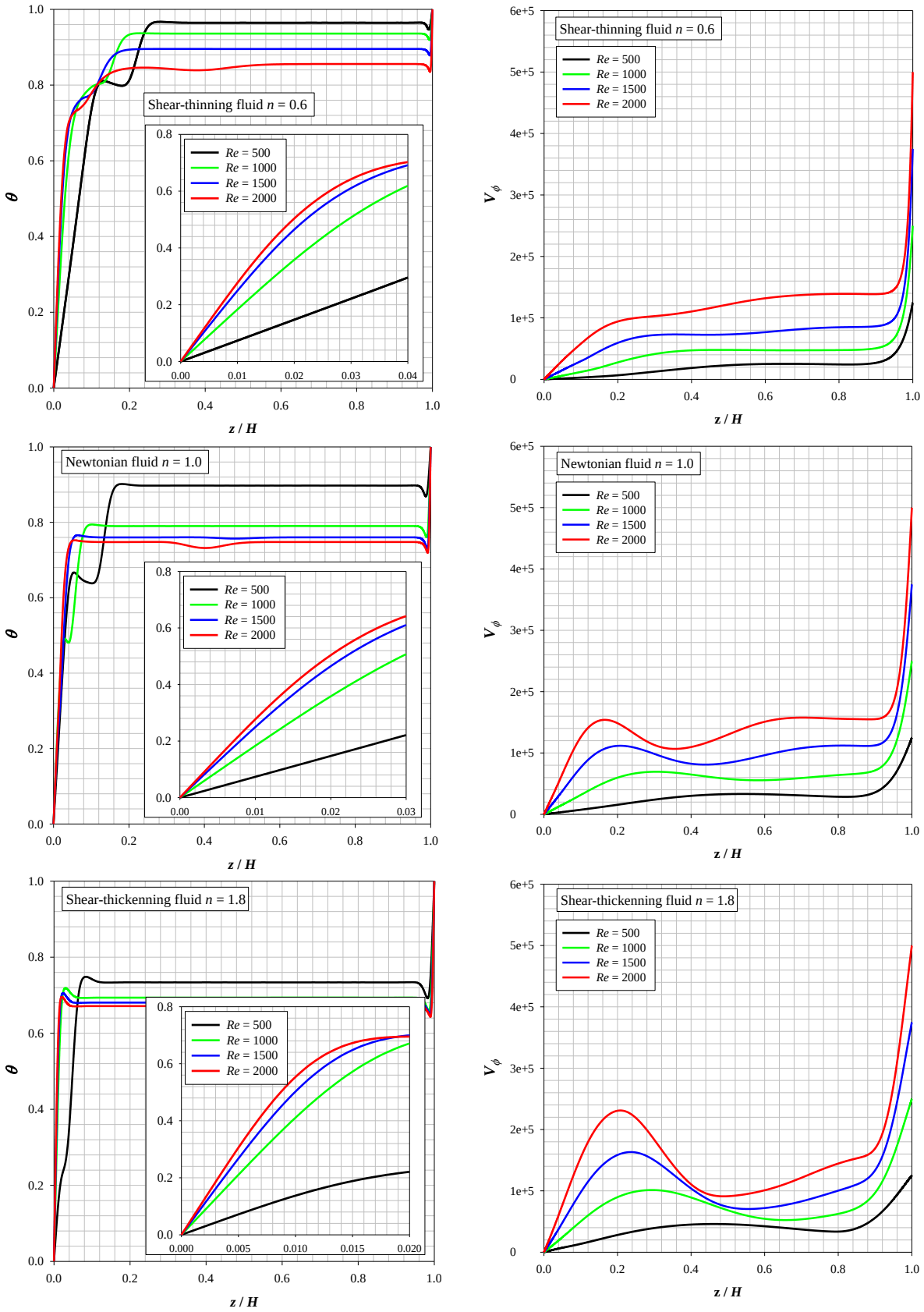

Fig. 3. The variation of non-dimensional temperature θ and swirl velocity component V_ϕ along the vertical mid-plane (i.e. r / R = 0.5) for different Re values for shear-thinning (i.e. $n = 0.6$), Newtonian (i.e. $n = 1$) and shear-thickening (i.e. $n = 1.8$) fluids cases at Ri = 0.5 and Pr = 500.

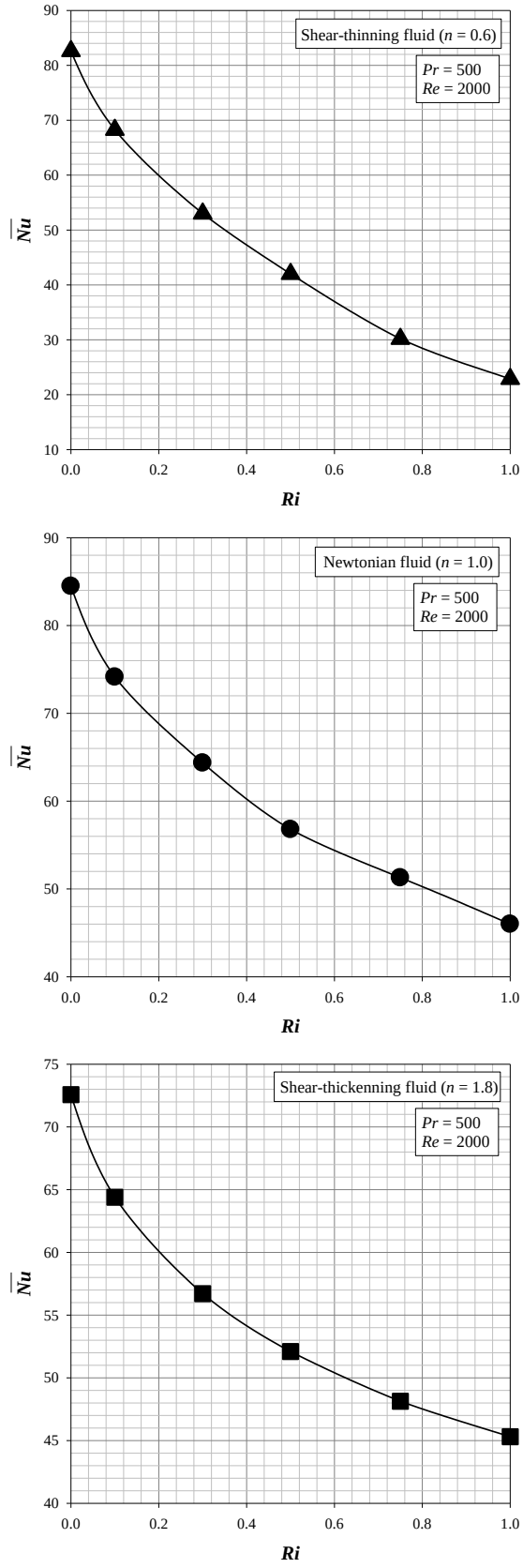

Fig. 4. The variation of mean Nusselt number $\overline{Nu}$ with Richardson number Ri in the case of shear-thinning (i.e. n = 0.6), Newtonian (i.e. n = 1) and shear-thickening (i.e. n = 1.8) fluids for Re = 2000 at Pr = 500.

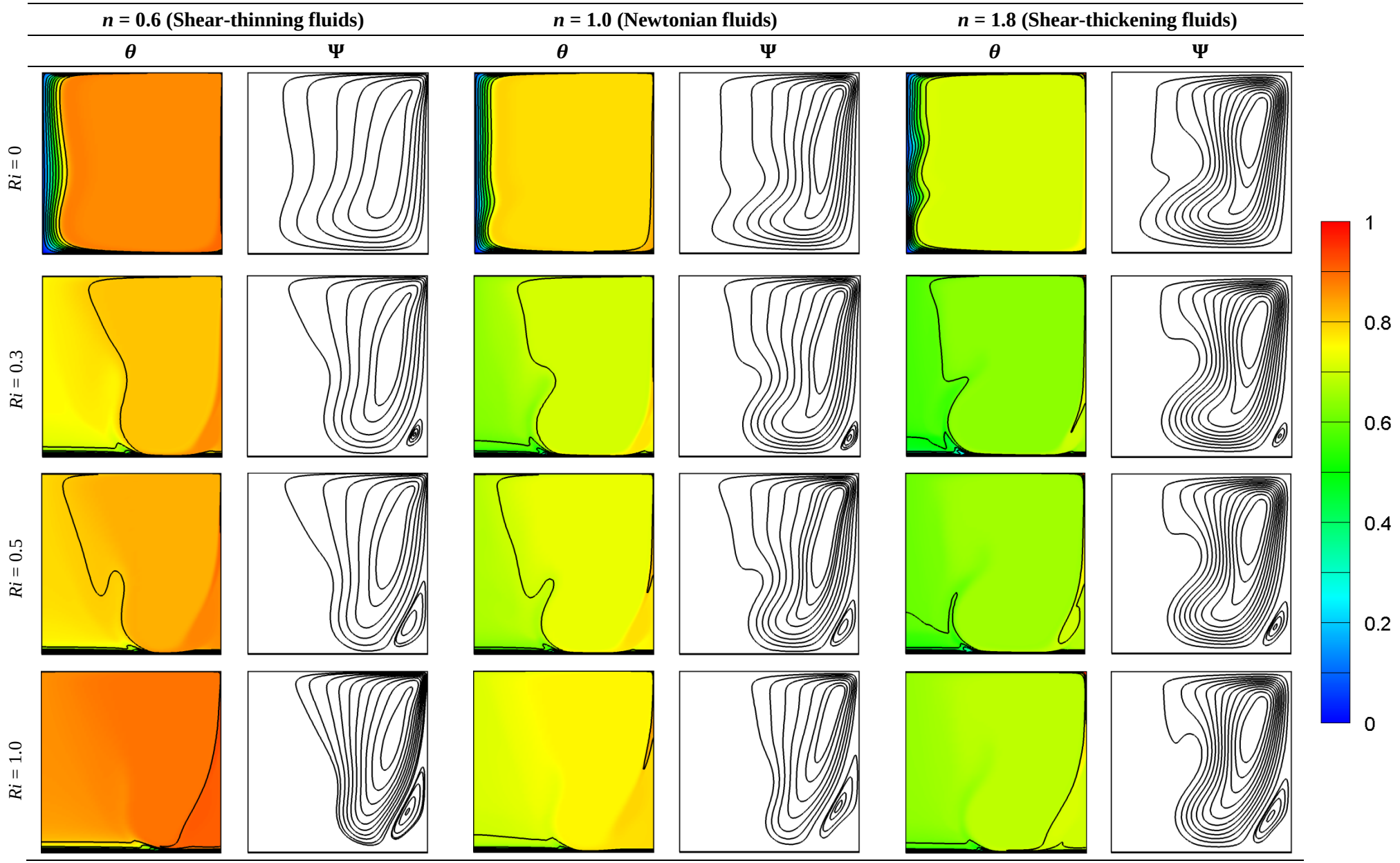

Fig. 5. Contours of non-dimensional temperature θ and stream functions (i.e. $\Psi = \psi/\alpha$) for different values of Ri at $Re = 2000$ and $Pr = 10^3$.

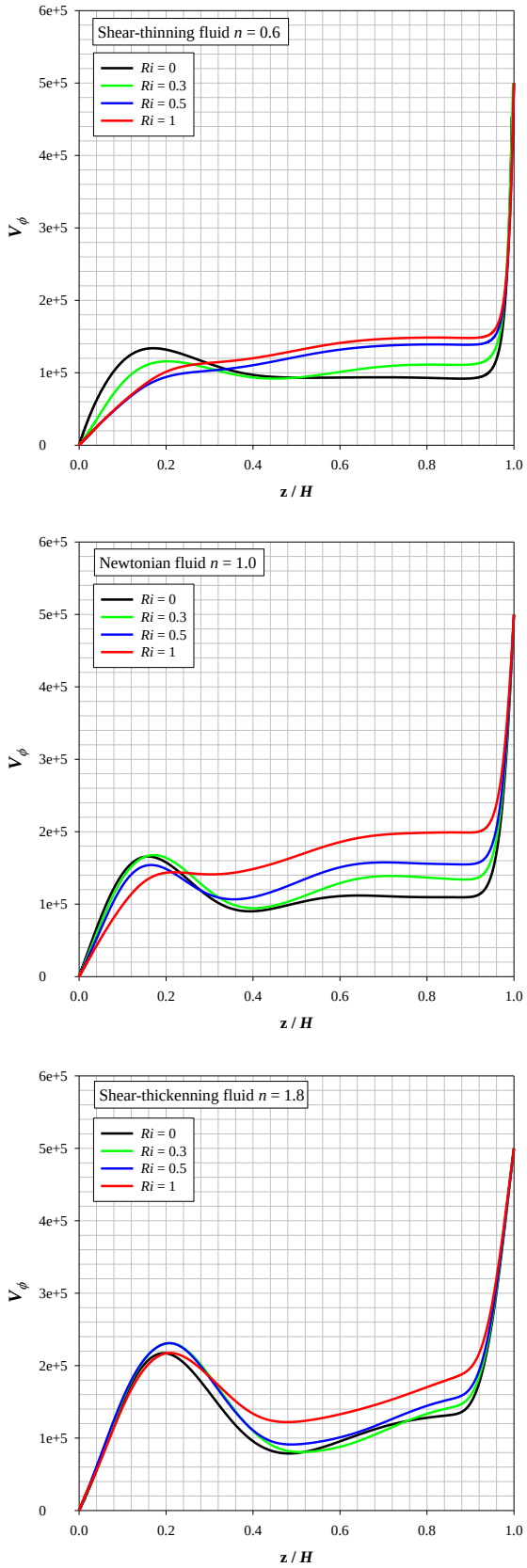

Fig. 6. The variation of non-dimensional temperature θ and swirl velocity component V_ϕ along the vertical mid-plane (i.e. r / R = 0.5) for different Ri values for shear-thinning (i.e. $n = 0.6$), Newtonian (i.e. $n = 1$) and shear-thickening (i.e. $n = 1.8$) fluids cases at Re = 2000 and Pr = 500.

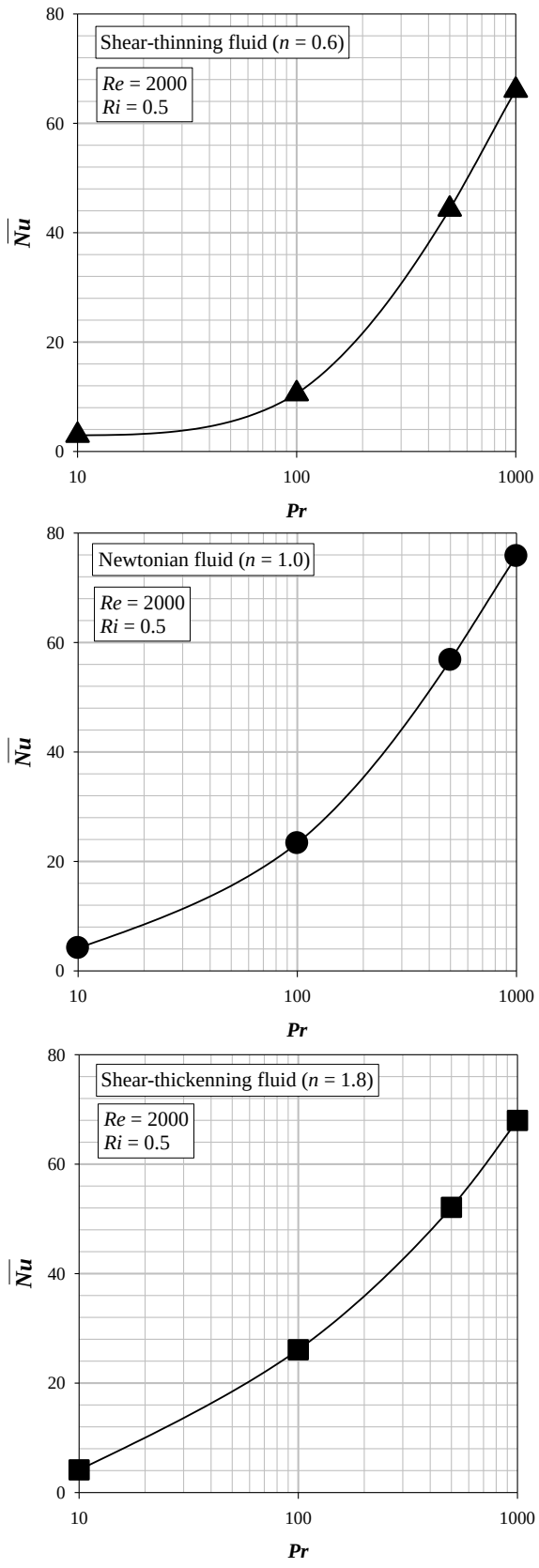

Fig. 7. The variation of mean Nusselt number $\overline{Nu}$ with Prandtl number Pr in the case of shear-thinning (i.e. n = 0.6), Newtonian (i.e. n = 1) and shear-thickening (i.e. n = 1.8) fluids for Ri = 0.5 at Re = 2000.

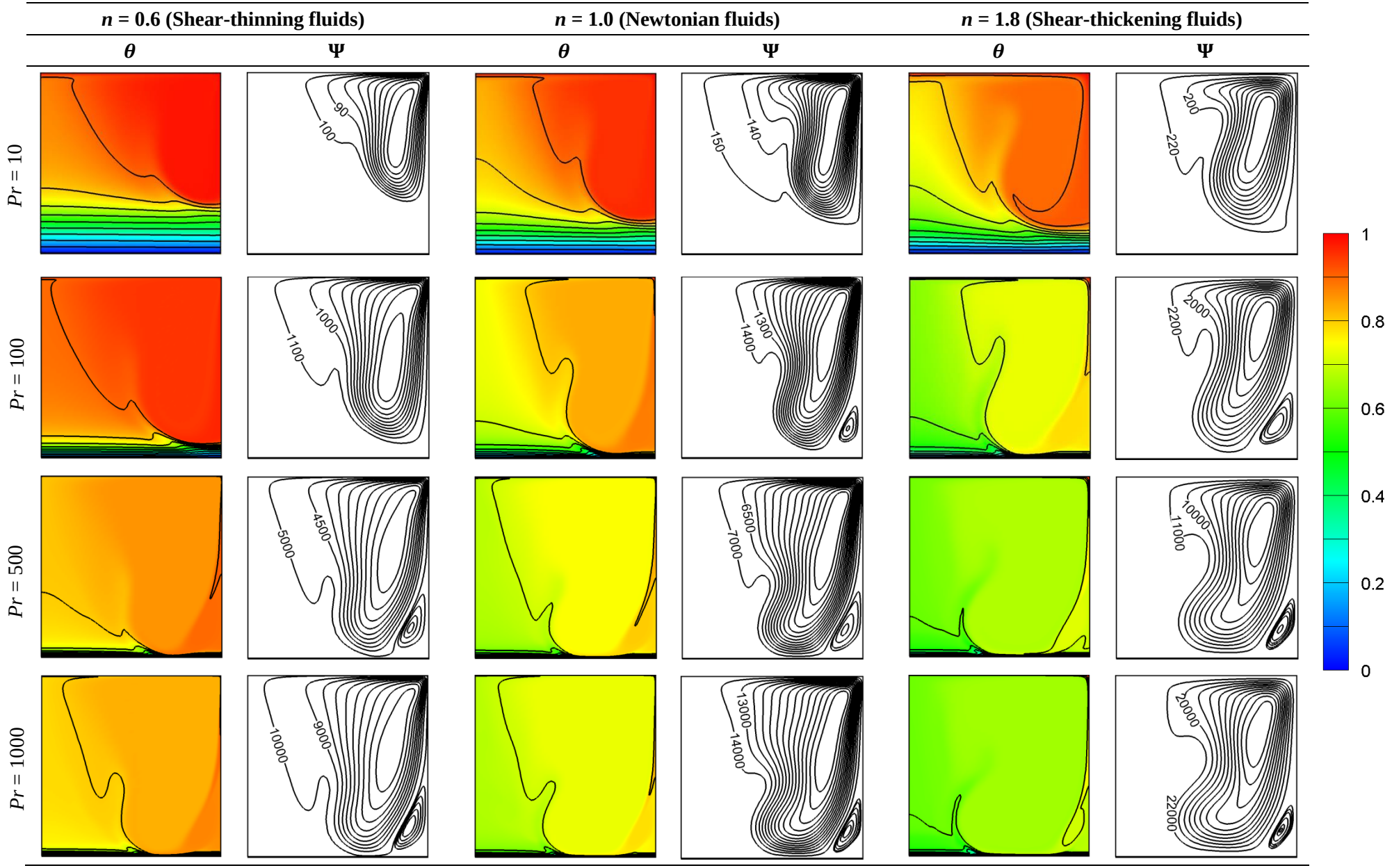

Fig. 8. Contours of non-dimensional temperature θ and stream functions (i.e. Ψ) for different values of Pr at $Re = 2000$ and $Ri = 0.5$.

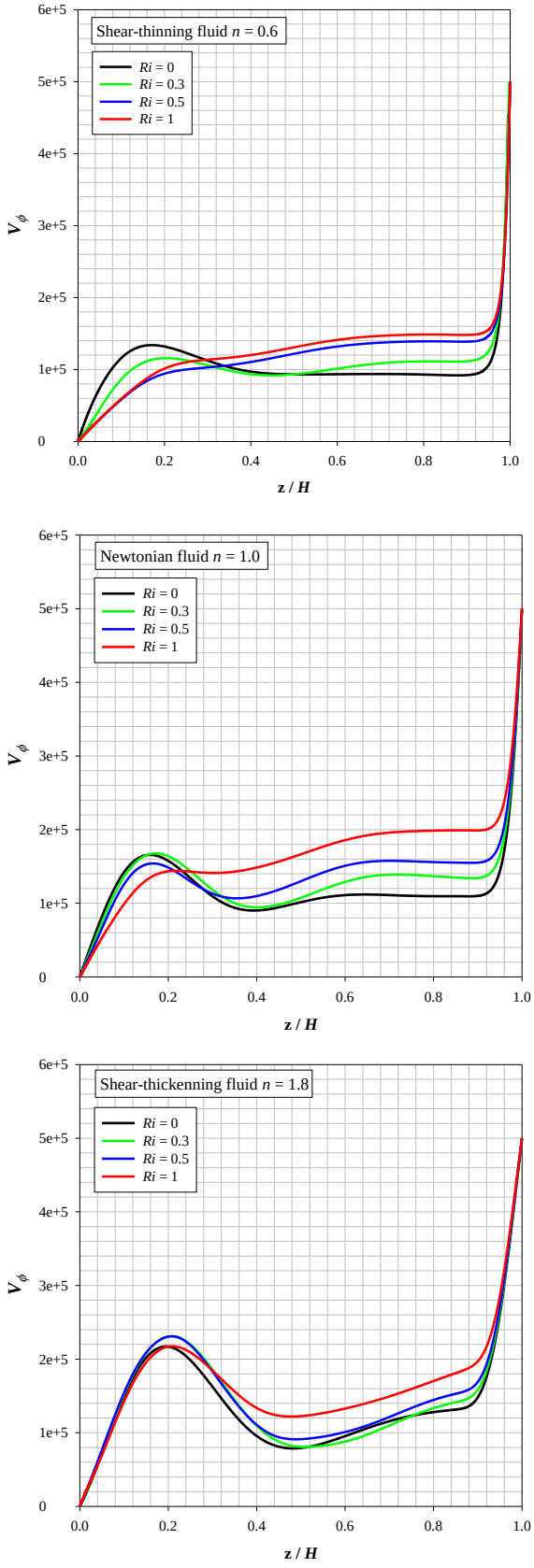

Fig. 9. The variation of non-dimensional swirl velocity component V_ϕ along the vertical mid-plane (i.e. r / R = 0.5) for different Pr values for shear-thinning (i.e. $n = 0.6$), Newtonian (i.e. $n = 1$) and shear-thickening (i.e. $n = 1.8$) fluids cases at $Ri = 0.5$ and $Re = 2000$.

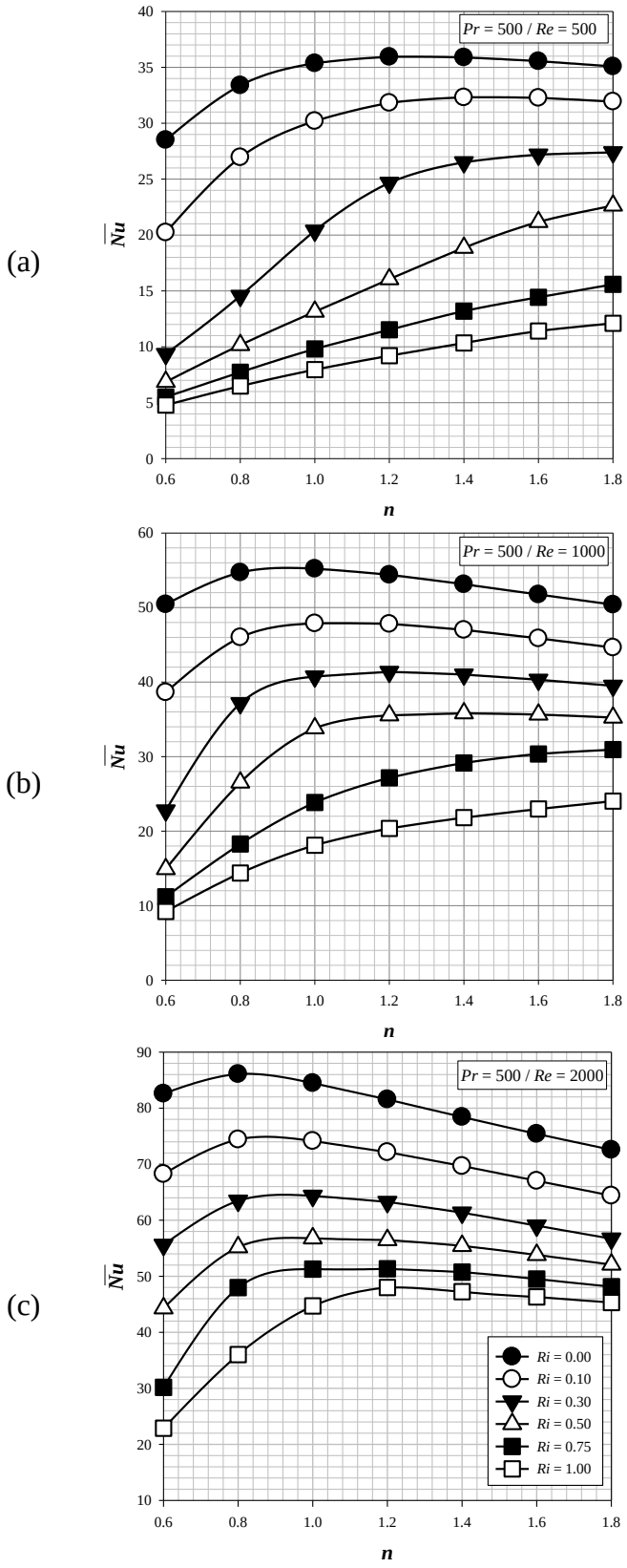

Fig. 10. The variation of mean Nusselt number $\overline{Nu}$ with power-law index n for different Ri values at Pr = 500: a) Re = 500, b) Re = 1000 and c) Re = 2000.

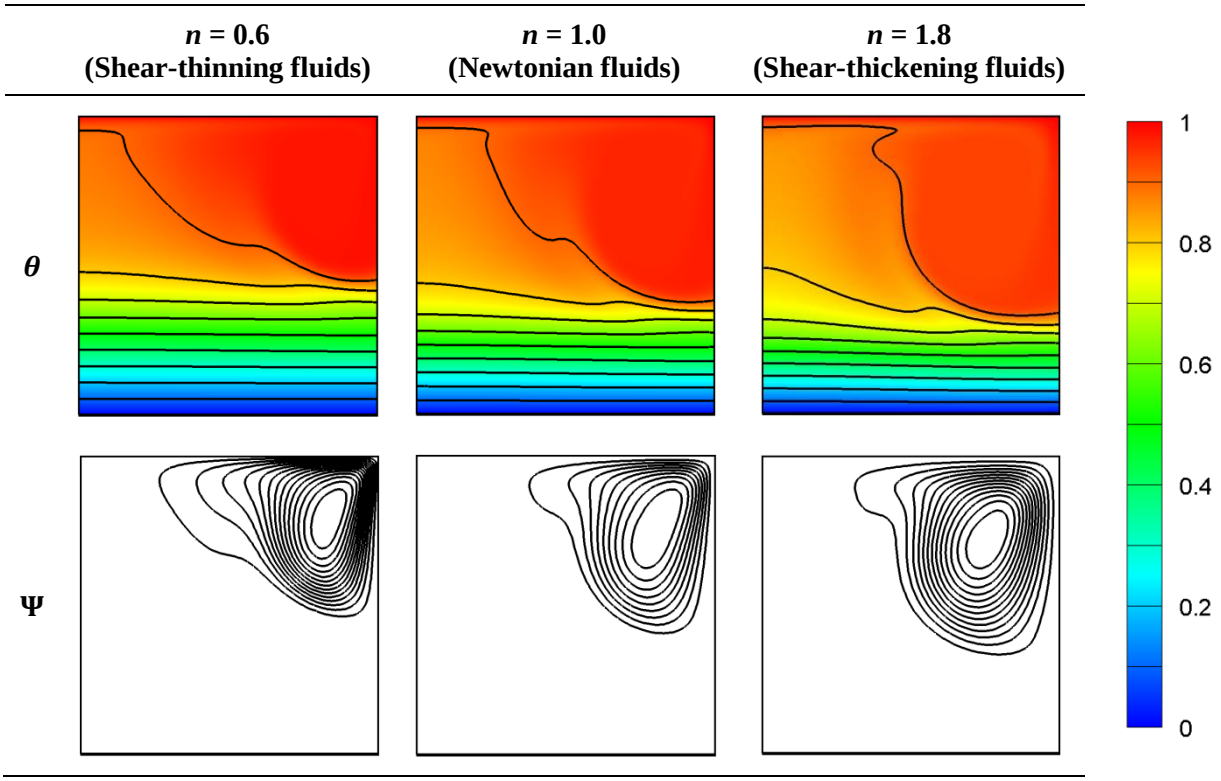

Fig. 11. Contours of non-dimensional temperature θ and stream functions (i.e. Ψ) for different n and values at $Re = 1000$, $Ri = 1.0$ and $Pr = 10$.

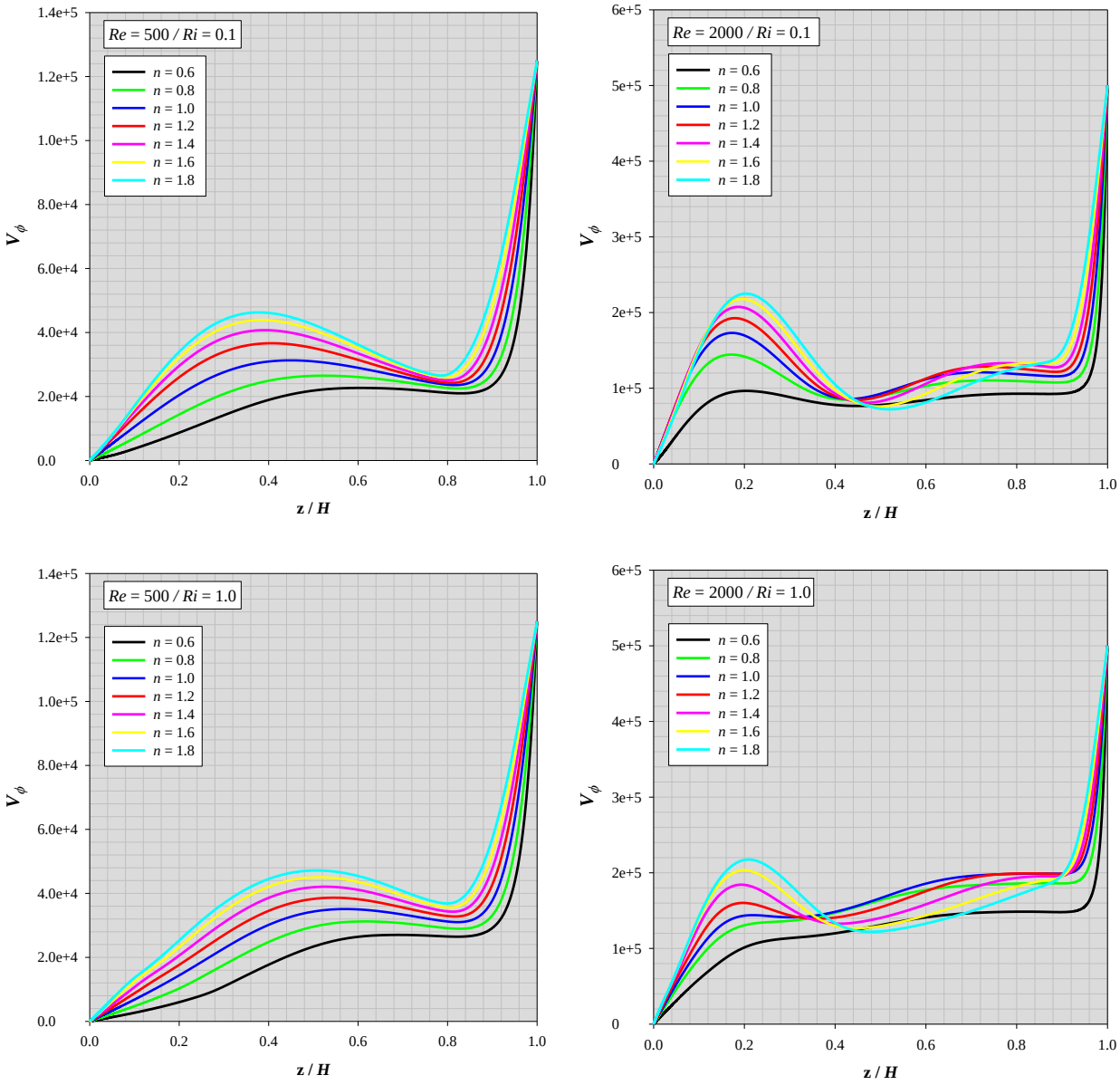

Fig. 12. The variation of non-dimensional swirl velocity component V_ϕ along the vertical mid-plane (i.e. r / R = 0.5) for different n values for $Re = 500$ (left column) 2000 (right column) for $Ri = 0.1$ and 1.0 at $Pr = 500$.

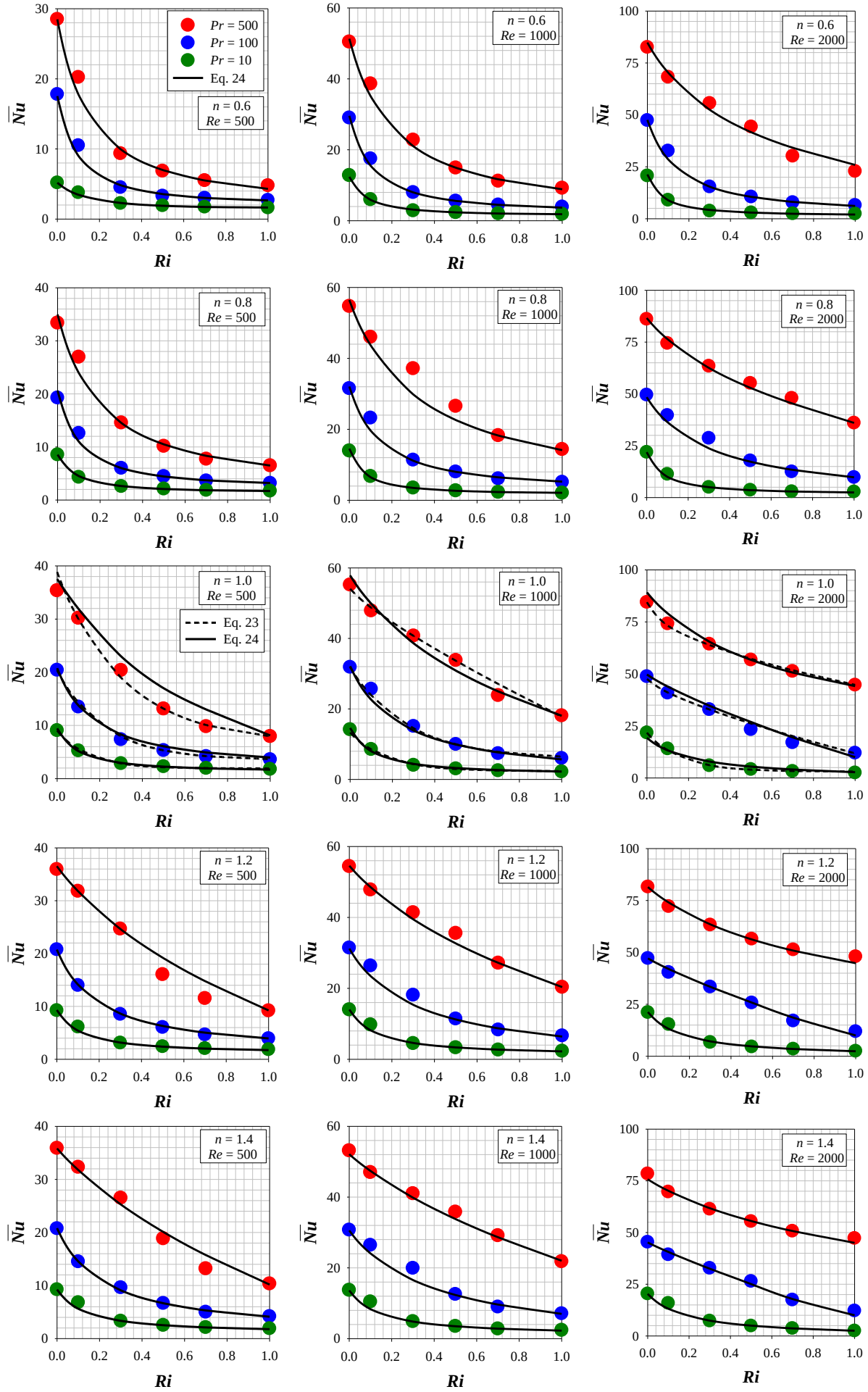

Fig. 13. Comparison between $\overline{Nu}$ obtained from the simulations with the predictions of Eq. 23 (only for Newtonian fluids) and 24 for both Newtonian (i.e. $n = 1$) and power-law fluids for different Ri, Re and Pr.